Metal–Organic Frameworks for Ammonia-Based Thermal Energy Storage

Guoliang An, Xiaoxiao Xia, Shaofei Wu, Zhilu Liu, Liwei Wang,* and Song Li*

Recently, the application of metal–organic frameworks (MOFs) in thermal energy storage has attracted increasing research interests. MOF-ammonia working pairs have been proposed for controlling/sensing the air quality, while no work has yet been reported on the immense potential of MOFs for thermal energy storage up till now. Herein, the feasibility of thermal energy storage using seven MOF-ammonia working pairs is experimentally assessed. From ammonia sorption stability and sorption thermodynamics results, it is found that MIL-101(Cr) exhibits both high ammonia sorption stability and the largest sorption capacity of ≈0.76 g g^{-1}. Compared with MIL-101(Cr)-water working pair, MIL-101(Cr)-ammonia working pair improves the sorption capacity by over three times with evaporation temperature lower than 8.4 °C. Due to stable ammonia sorption stability and negligible hysteresis, MIL-101(Cr) and ZIF-8(Zn) are tested at condensation/evaporation temperature of 30 °C/10 °C. The thermal energy storage density (reaching over 1200 kJ kg^{-1}) and coefficient of performance of MIL-101(Cr)-based system are both higher than ZIF-8(Zn)-based one due to larger average isosteric enthalpy and cycle sorption capacity. This experimental work paves the way for developing the high efficient and stable thermal energy storage system with MOF-ammonia working pairs especially for critical conditions with low evaporation temperature and high condensation temperature.

1. Introduction

Promoting efficiency of sustainable energy storage has been one of the top ten scientific challenges critical to human society development.[1] Since the widely existing low-grade thermal energy below 200 °C occupies typically 36–54% of the usable primary energy,[2,3] its rational utilization can relieve the inconsistency between insufficient thermal energy supply and the growing thermal energy demand.

Typical thermal energy storage materials can be generally classified into sensible heat materials,[4] phase change materials,[5] absorption working pairs,[6] and solid sorption working pairs.[7] Among them, solid sorption has the merits of relatively high thermal energy storage density and low heat loss during storage phase.[8] Solid sorption can be divided into physical adsorption caused by van de Walls force and chemisorption dominated by complex reaction or oxidation reaction.[9] Although the sorption capacity of conventional pure chemical sorbents is large, its expansion and agglomeration together with the low thermal conductivity and permeability lead to the serious degradation of cycle sorption and thermal energy utilization performance.[10] Meanwhile, too low sorption capacity of pure physical sorbents results in the ultra large volume of the whole system in practical applications. The development of composite sorbents is a breakthrough in the field of advanced sorbents. Expanded natural graphite (ENG) and its upgraded version treated by sulfuric acid (ENG-TSA) aim at preventing agglomeration and enhancing heat and mass transfer.[11] Most matrix (e.g., activated carbon, activated carbon fiber, silica gel, carbon nanotubes) based on their moderate porous structures can improve the heat and mass transfer and adjust the sorption performance for chemisorption of composite sorbents simultaneously.[12]

Besides conventional composite sorbents for thermal energy storage, porous metal–organic frameworks (MOFs) have been promoted rapidly in recent decades, even though their initial applications are focused on gas storage and separation,[13] catalysis,[14] molecule sensing,[15] and drug delivery.[16] High crystalline state, large porosity and surface area, flexible framework, available specific structure and function by reasonable molecular design, facile chemical modification and synthesis assembly methods are advantages of MOFs. However, the relative low thermal and chemical stability compared with conventional porous carbon and zeolites limit their applications.[17,18]

After ISE-1 was proposed as the first MOF candidate for thermal energy storage materials in 2009,[19] a series of MOFs have received increasing attention in this field, especially with water as the sorbate.[20–22] Up till now, many studies have

G. An, S. Wu, L. Wang
Institute of Refrigeration and Cryogenics
Key Laboratory of Power Machinery and Engineering of MOE
Shanghai Jiao Tong University
Shanghai 200240, China
E-mail: lwwang@sjtu.edu.cn
X. Xia, Z. Liu, S. Li
State Key Laboratory of Coal Combustion
School of Energy and Power Engineering
Huazhong University of Science and Technology
Wuhan 430074, China
E-mail: songli@hust.edu.cn

contributed to the development of MOF-based thermal energy utilizations. de Lange et al. proposed the potential of MOFs on solid sorption-driven heat pumps with CAU-10(Al)-H, MIL-101(Cr), MIL-100(Fe), Al-fumarate, MOF-841(Zr), MOF-801(Zr), MIL-53(Cr), and Zn(BDC)(DABCO)$_{0.5}$ as candidates due to their high stability for water or ethanol sorbates.[23] Chaechuen et al. overviewed promising MOFs with tunable porosity and the hydrophilic/hydrophobic design for heat transformation applications using water as sorbate.[24] Makhanya et al. reviewed the application of MOFs for sorption thermal energy storage through evaluation of recent developments and identified strategies to improve MOF performance.[25] MOFs with high water sorption capacity (such as MIL-101(Cr)) commonly exhibit type S isotherms,[23] which means their water sorption capacity will reduce dramatically under critical conditions of low evaporation temperature and high condensation temperature, resulting lower practical thermal energy storage density.

Except for water, ammonia is also a promising sorbate which has been widely applied for solid sorption-driven thermal energy utilizations, and promoted for commercial applications especially after coupled with a series of halides.[26] Even though MOF-ammonia working pairs have ever been referred to the potential application in heat pumps,[23] no useful candidate has been reported because of the lacking ammonia sorption data at relevant conditions. Until now, no reports on ammonia uptake by MOFs aiming at thermal energy storage have been reported except for controlling[27–29] or sensing the air quality.[30–32] In most cases, ammonia sorption capacities are measured by breakthrough experiments at ambient pressure with ammonia diluted with dry air or moist air.[27] Rieth et al. designed a series of mesoporous MOFs with coordinatively unsaturated metal sites, which own high and reversible ammonia sorption capacities., that is, 15.47, 12.00, and 12.02 mmol g^{-1} of isostructural Mn, Co, and Ni materials, respectively.[33] Furthermore, Rieth et al. reported that a series of microporous triazolate MOFs containing open metal-sites exhibit record static and dynamic ammonia capacities. Under equilibrium conditions at 1 bar, the ammonia capacity can reach up to 19.79 mmol g^{-1}, while under conditions relevant to personal protection equipment, the ammonia capacity can reach 8.56 mmol g^{-1}.[34] Liu et al. examined the ammonia sorption behavior of several versions of an archetypal zirconium-based MOF material, which provides insights into the chemical basis for both reversible and irreversible sorption of ammonia by Zr-MOFs and related compounds.[32] The effects of water on ammonia sorption have been widely investigated and summarized such as causing the collapse of MOF structure,[35] increasing sorption capacities via dissolution of extra ammonia[36] or competing against ammonia for active sites.[37] However, saturated ammonia (liquid phase and gas phase) as sorbate, which is isolated from atmospheric environment and without moisture, is generally utilized for thermal energy storage. But there are few studies on MOF-ammonia working pairs for thermal energy storage.

In this work, we elaborately assessed the feasibility of MOF-ammonia working pairs for solid sorption-driven thermal energy storage. After demonstrating the mechanisms of ammonia sorption in MOFs, the ammonia sorption stability of targeted MOFs was discussed. Subsequently, MOF candidates were selected considering the hysteresis characteristics and sorption capacity under the premise of their high ammonia stability. The

thermodynamic efficiency and thermal energy storage density of these MOFs for thermal energy storage were determined, followed by the comprehensive summary.

2. Principle

Similar to water sorption, three different mechanisms for ammonia capture in MOFs can be summarized: sorption on the metal ions (irreversible), cluster or layer sorption (reversible) and capillary condensation (irreversible) in pores.[38] For MOFs with coordinatively unsaturated sites on the metal ions, ammonia molecules can be clustered and irreversibly sorbed by those sites to modify the coordination sphere. As most MOFs consist of hydrophobic aromatic ligands, cluster sorption is preferential to the layer formation, while the high polar functional groups (such as $-OH$, $-NH_2$, $-COOH$, $-SO_3H$) can be attached to the organic ligands and act as additional nucleation sites for clustering ammonia by hydrogen bonds. Theoretically, the critical pore diameter (D_c) expressed in Equation (1) determines the occurrence of irreversible capillary condensation:[39]

$$D_c = 4\sigma T_c / (T_c - T) \tag{1}$$

where σ is the kinetic diameter of sorbate molecule (2.9 Å for ammonia), T_c is the critical temperature (405.7 K for ammonia), T is the actual temperature. Therefore, this theory yields the critical diameter of 44 Å for ammonia at room temperature. For the pore diameters of MOFs smaller than D_c, ammonia sorption occurs solely by the cluster/layer formation, whereas for the pore diameters larger than D_c, ammonia will be sorbed due to capillary condensation which results in hysteresis between adsorption and desorption processes, preceded by cluster/layer sorption.

Seven representative MOFs, that is, MIL-101(Cr), MIL-100(Fe), ZIF-8(Zn), Cu-BTC, UiO-66(Zr), NU-1000(Zr), and DUT-67(Zr) are selected for ammonia sorption. The crystal structure and simulated pore size distribution (PSD) of these selected MOFs are shown in **Figure 1**. MIL-101(Cr) and MIL-100(Fe) are both 3D caged structures composed of six-ring cages (L-cage) and five-ring cages (S-cage).[40] ZIF-8(Zn), Cu-BTC, UiO-66(Zr), and DUT-67(Zr) belong to cubic crystal system, and NU-1000(Zr) can be classified into hexagonal crystal system. Pore diameters of all selected MOFs are smaller than D_c, thus ammonia capillary condensation will not occur theoretically. Among these MOFs, the ammonia sorption stability of MIL-101(Cr),[41] ZIF-8(Zn),[42] and UiO-66(Zr)[43] has been verified under low pressure within 1 bar, but the structure of Cu-BTC is not reversible after ammonia sorption.[44] The ammonia sorption stability of MIL-100(Fe), NU-1000(Zr), and DUT-67(Zr) has not ever been investigated.

3. Results and Discussion

3.1. Ammonia Sorption Stability

Ammonia sorption stability is a perquisite for ammonia-based thermal energy storage application. Commonly, three to five
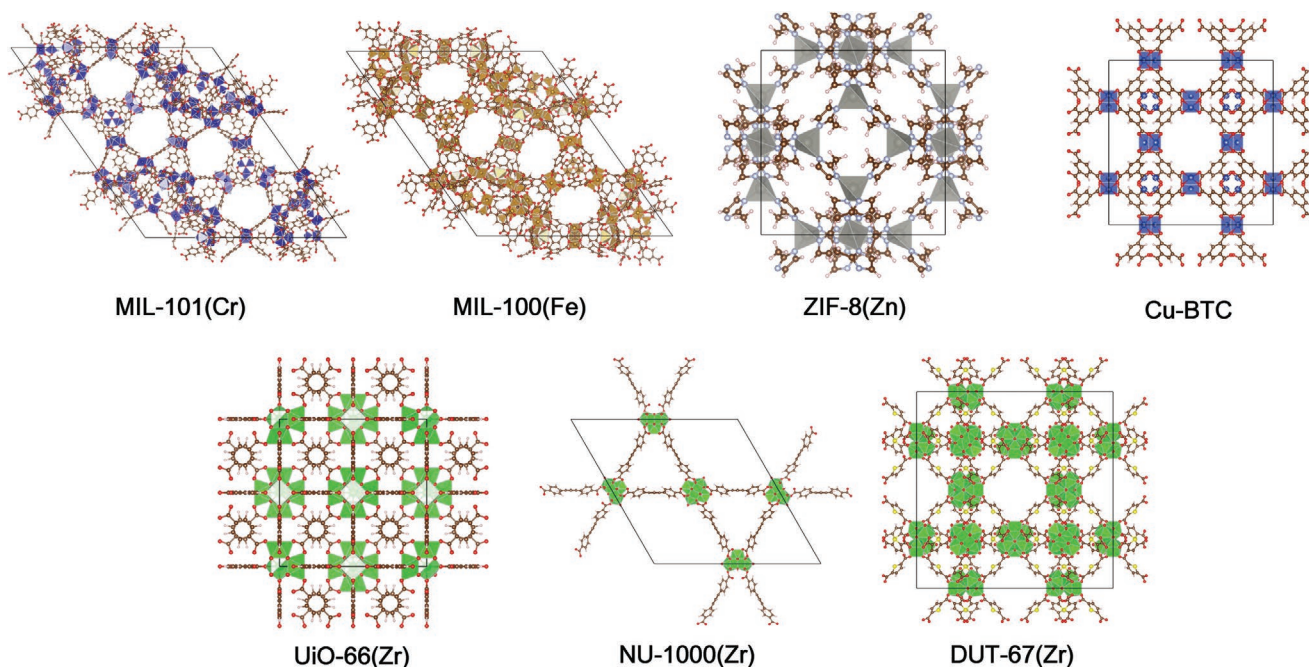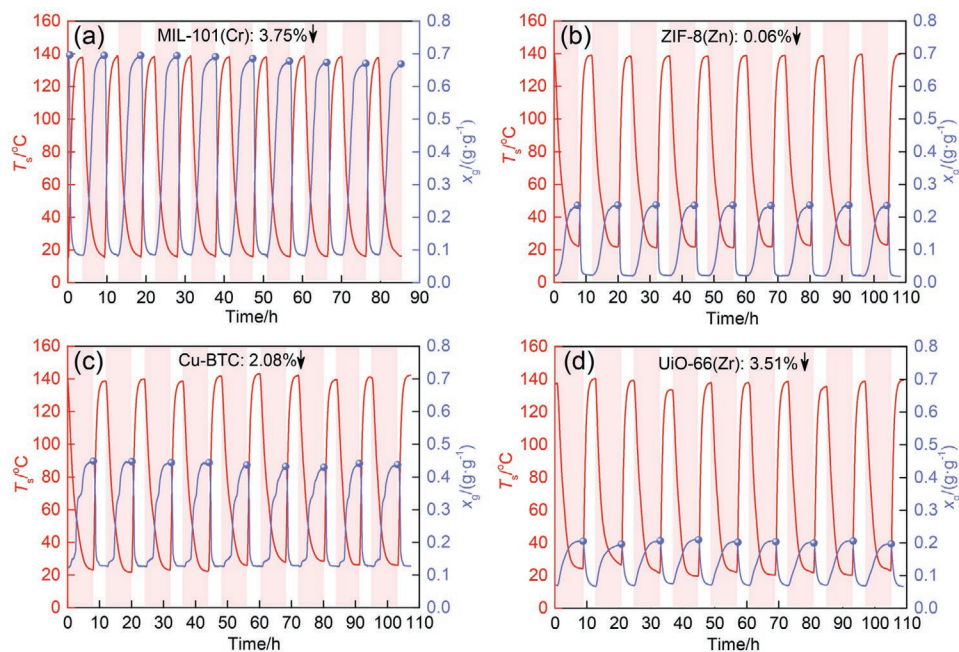
Figure 1. The crystal structures and simulated PSD of MIL-101(Cr), MIL-100(Fe), ZIF-8(Zn), Cu-BTC, UiO-66(Zr), NU-1000(Zr), and DUT-67(Zr).
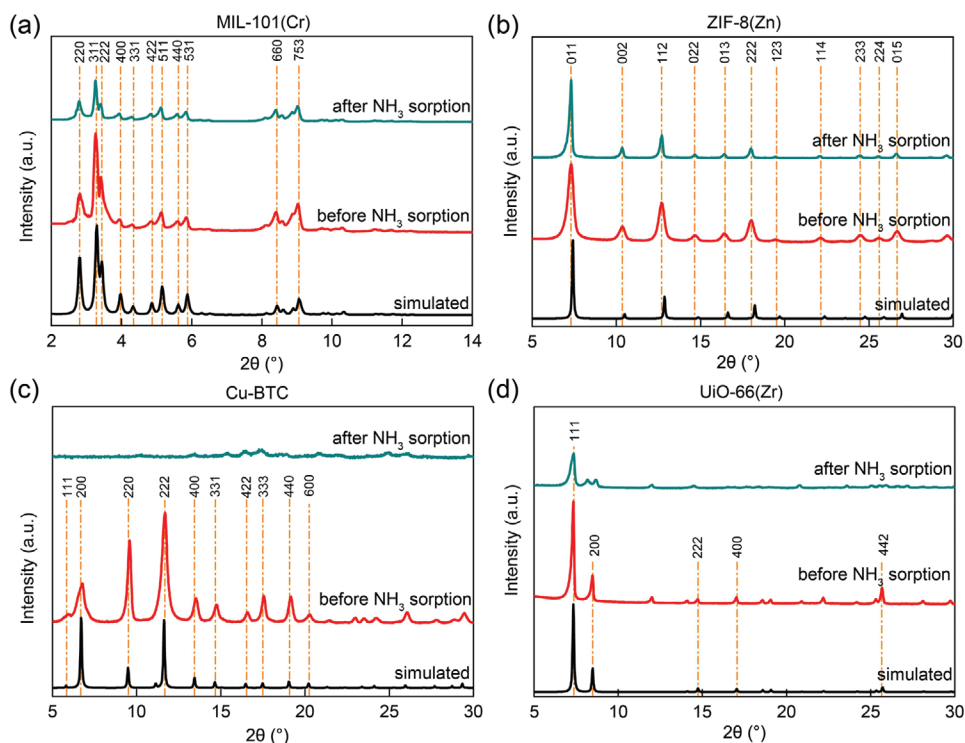
sorption cycles were required in order to test the sorption stability of ammonia sorption.[41,45] In this part, nine cycles were carried out to research the ammonia sorption recyclability of MOFs. As shown in **Figure 2**, MIL-101(Cr), ZIF-8(Zn), Cu-BTC, and UiO-66(Zr) exhibited high ammonia sorption stability and recyclability under saturated ammonia, whose maximum sorption capacities were only reduced by 3.75%, 0.06%, 2.08%, and 3.51% after nine cycles, respectively. In contrast, MIL-100(Fe),

NU-1000(Zr), and DUT-67(Zr) were unstable in ammonia atmosphere (Figure S1, Supporting Information). The maximum sorption capacities of MIL-100(Fe), NU-1000(Zr), and DUT-67(Zr) were decreased by 32.4%, 26.2%, and 65.3%.

Ammonia sorption stability was characterized by powder X-ray diffraction (PXRD), scanning/transmission electron microscope (SEM/TEM), nitrogen adsorption (at 77 K), and Fourier transform infrared spectroscopy (FT-IR). The detailed

Figure 2. Ammonia sorption stability of a) MIL-101(Cr), b) ZIF-8(Zn), c) Cu-BTC, d) UiO-66(Zr) at 6.1 bar.

ADVANCED
SCIENCE NEWS
www.advancedsciencenews.com

NANO · MICRO
small
www.small-journal.com

Figure 3. PXRD patterns of a) MIL-101(Cr), b) ZIF-8(Zn), c) Cu-BTC, d) UiO-66(Zr) simulated (black), before (red) and after (green) NH$_3$ sorption.
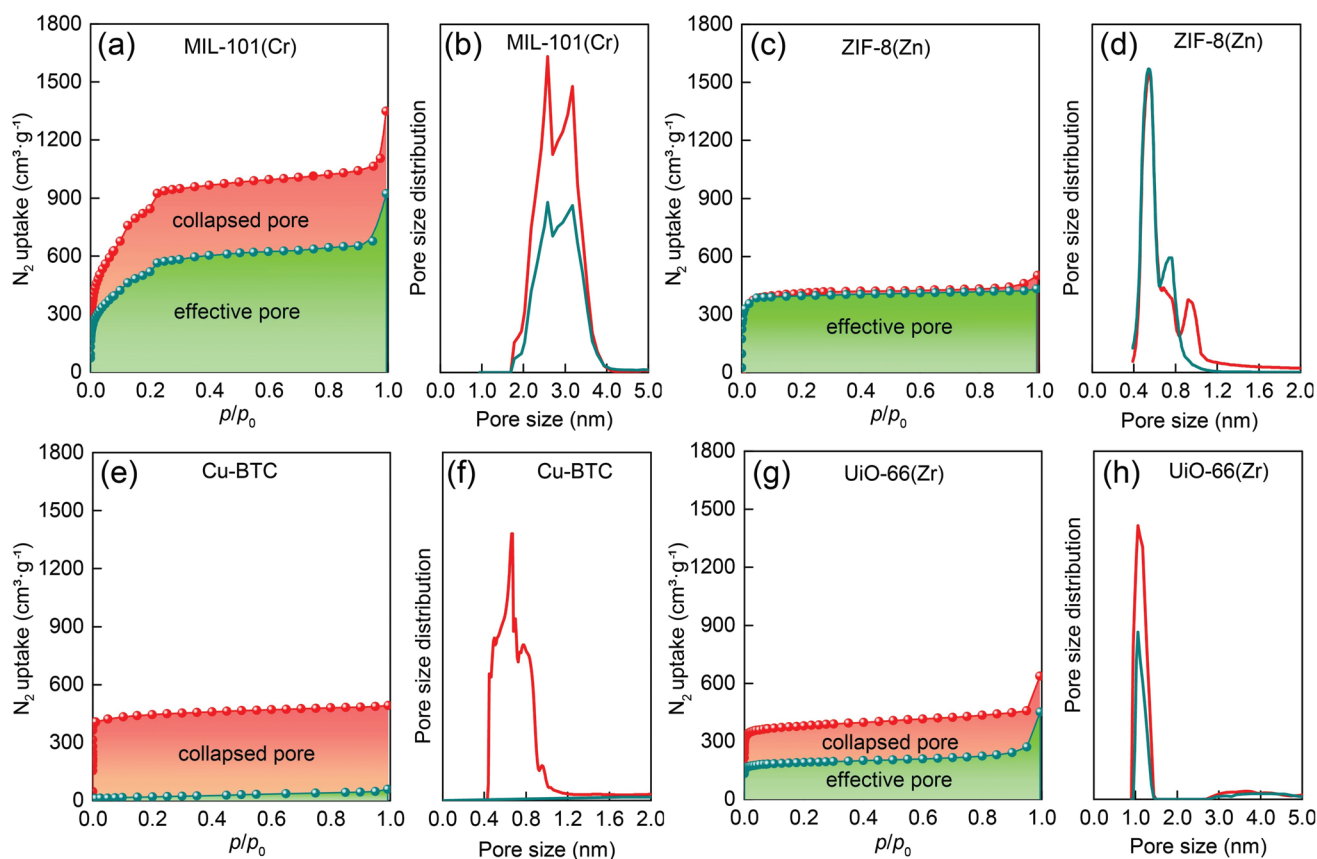
characterization results of MIL-101(Cr), ZIF-8(Zn), Cu-BTC, and UiO-66(Zr) exhibiting good ammonia sorption stability before and after ammonia sorption are analyzed in **Figures 3–6**.

PXRD pattern of samples before and after ammonia sorption presented in Figure 3 shows that the crystallinity was partially (MIL-101(Cr) and UiO-66(Zr), Figure 3a–d) or fully (ZIF-8(Zn), Figure 3b) preserved, except for Cu-BTC (Figure 3c). The

location and intensity of peaks in PXRD pattern of ZIF-8(Zn) did not change upon ammonia sorption, indicating the excellent ammonia sorption stability of ZIF-8(Zn). MIL-101(Cr) and UiO-66(Zr) lost partial crystallinity with the decreased intensity in PXRD pattern, especially for UiO-66(Zr). Moreover, the peaks in (111) and (442) of UiO-66(Zr) disappeared after ammonia sorption, further indicating MIL-101(Cr) was more
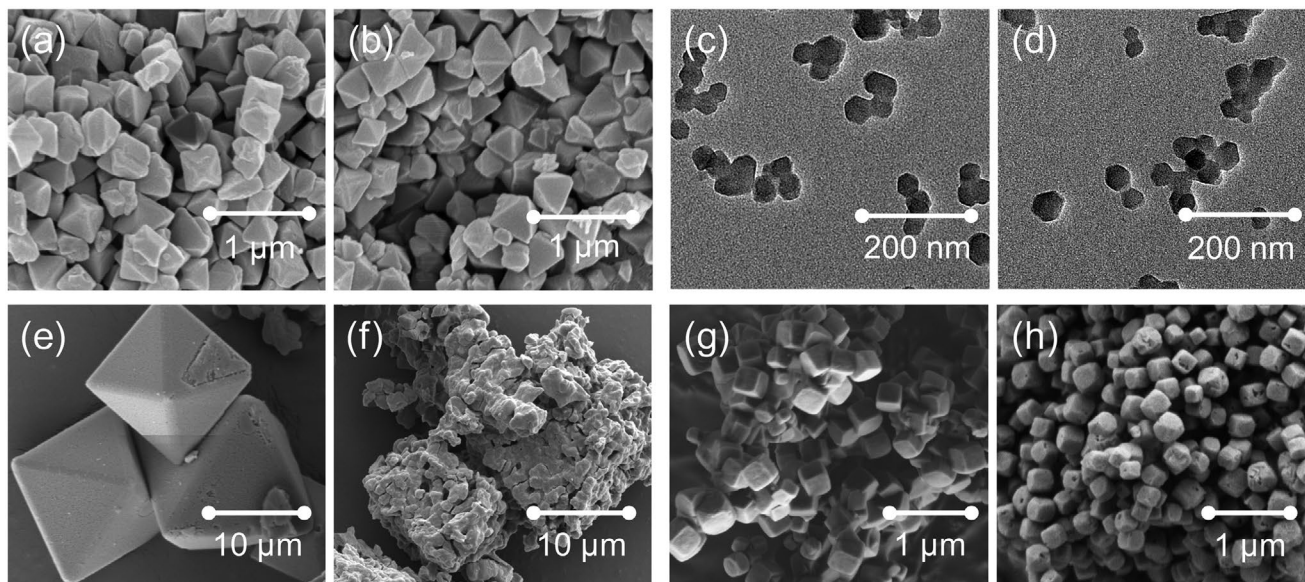
Figure 4. SEM/TEM images: a) MIL-101(Cr) before NH$_3$ sorption, b) MIL-101(Cr) after NH$_3$ sorption, c) ZIF-8(Zn) before NH$_3$ sorption, d) ZIF-8(Zn) after NH$_3$ sorption, e) Cu-BTC before NH$_3$ sorption, f) Cu-BTC after NH$_3$ sorption, g) UiO-66(Zr) before NH$_3$ sorption, h) UiO-66(Zr) after NH$_3$ sorption.

ADVANCED
SCIENCE NEWS
www.advancedsciencenews.com

NANO · MICRO
small
www.small-journal.com

Figure 5. Nitrogen uptake at 77 K of a) MIL-101(Cr), c) ZIF-8(Zn), e) Cu-BTC, g) UiO-66(Zr) and PSD at 77 K of b) MIL-101(Cr), d) ZIF-8(Zn), f) Cu-BTC, h) UiO-66(Zr) before (red) and after (green) NH_3 sorption, where the effective pore region represents the area below "after NH_3 sorption" points, and the collapsed pore region represents the area between "before NH_3 sorption" points and "after NH_3 sorption" points.

stable than UiO-66(Zr) in ammonia atmosphere. Cu-BTC was unstable with the absence of all peaks after ammonia sorption.

Consistent with the SEM/TEM images, the morphology of MIL-101(Cr) (Figure 4a,b) and ZIF-8(Zn) (Figure 4c,d) did not show any obvious change. However, the octahedral structure of Cu-BTC (Figure 4e) was destroyed after ammonia sorption (Figure 4f). In contrast, UiO-66(Zr) still maintained a hexahedral structure, while the surface became rough and defective (Figure 4h) after ammonia sorption.

In order to characterize the effect of ammonia sorption on the porosity of MOFs, N_2 adsorption isotherms of MOFs at 77 K were measured (Figure 5a,c,e,g, where the effective pore region represents the area below "after NH_3 sorption" points, and the collapsed pore region represents the area between "before NH_3 sorption" points and "after NH_3 sorption" points). BET surface area, total pore volume and PSD from N_2 adsorption isotherms are shown in Table S1, Supporting Information, and Figure 5b,d,f, h). The N_2 uptake of MIL-101(Cr) was reduced with the decrease of BET surface area and total pore volume after ammonia sorption (Figure 5a and Table S1, Supporting Information), indicating that ammonia imposed negative impacts on the framework of MIL-101(Cr). Meanwhile, it can be seen from the PSD of MIL-101(Cr) that the pore size did not change, while total pore volume was reduced (Figure 5b). There was no obvious change on N_2 uptake, BET surface area

and pore volume (Figure 5c and Table S1, Supporting Information), indicating that the porosity of ZIF-8(Zn) was retained after ammonia sorption, consistent with PSD of ZIF-8(Zn) (Figure 5d). The porosity of Cu-BTC was fully destroyed after ammonia sorption with its remarkable reduced N_2 uptake (Figure 5e), BET surface area (Table S1, Supporting Information), total pore volume (Table S1, Supporting Information) and pore size (Figure 5f) of Cu-BTC. For instance, the BET surface area and total pore volume of Cu-BTC dropped from 1756.0 to 71.6 m² g⁻¹ and from 0.764 to 0.091 cm³ g⁻¹, respectively. However, the ammonia uptake of Cu-BTC did not reduce after 9 cycle sorption (Figure 2c), so the ammonia sorption capacity of Cu-BTC may be contributed by chemisorption between ammonia and unsaturated metal sites of Cu-BTC but not the pore structure. Similar to MIL-101(Cr), almost one half of N_2 uptake (Figure 5g), BET surface area (Table S1, Supporting Information), total pore volume (Table S1, Supporting Information) of UiO-66(Zr) were reduced after ammonia sorption, except for pore size (Figure 5h). On the whole, the porosity of ZIF-8(Zn) was maintained, while the porosity of other MOFs was reduced part partially or fully. Considering the fact that all these MOFs have stable ammonia sorption capacity, FT-IR spectra is necessary to verify the contribution of chemisorption and physical adsorption on the ammonia sorption capacity.
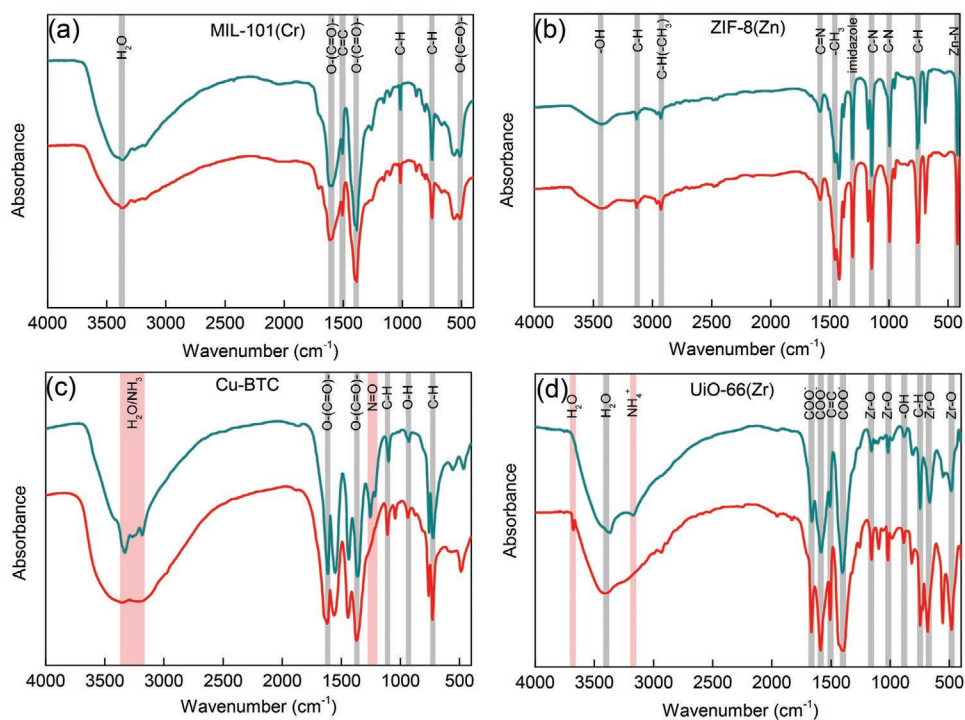
Figure 6. FT-IR spectra of a) MIL-101(Cr), b) ZIF-8(Zn), c) Cu-BTC, d) UiO-66(Zr) before (red) and after (green) NH_3 sorption.

Results of FT-IR spectra of MOFs are shown in Figure 6, with new peaks highlighted as red region. As no new bond on FT-IR spectra (Figure 6a,b) resulting from ammonia sorption was noticeable compared to as-synthesized MIL-101(Cr) (Figure 6a) and ZIF-8(Zn) (Figure 6b), it can be inferred that no chemisorption occurred and the structures did not show obvious damage after ammonia sorption, especially for ZIF-8(Zn). Unsaturated metal sites in MIL-101(Cr) and metal ions in ZIF-8 are the primary active sites for ammonia adsorption. The hydrophobicity and stability of ZIF-8 have been repeatedly reported for water sorption. The polarity of water and ammonia are both larger than sorbates like CO_2 and H_2 because of hydrogen bonds. The fact that ZIF-8 is most stable for ammonia sorption among the investigated MOFs proves that hydrophobicity plays a positive role in MOFs stability. New bonds appeared at 3269, 3184, 1254, and 1215 cm^{-1} in FT-IR spectra of Cu-BTC after ammonia sorption (Figure 6c), among which 3269 and 3184 cm^{-1} were attributed to the vibration of ammonia molecules, while 1254 and 1215 cm^{-1} may relate to the new component $(NH_4)_3BTC$ (the carboxylate groups from BTC react with ammonia),[36,46] indicating the chemical instability of Cu-BTC in ammonia. New bonds in FT-IR spectra of UiO-66(Zr) were attributed to protonated NH_3, which may result from the reaction between NH_3 and the presence of impurities (water or DMF) in UiO-66(Zr).
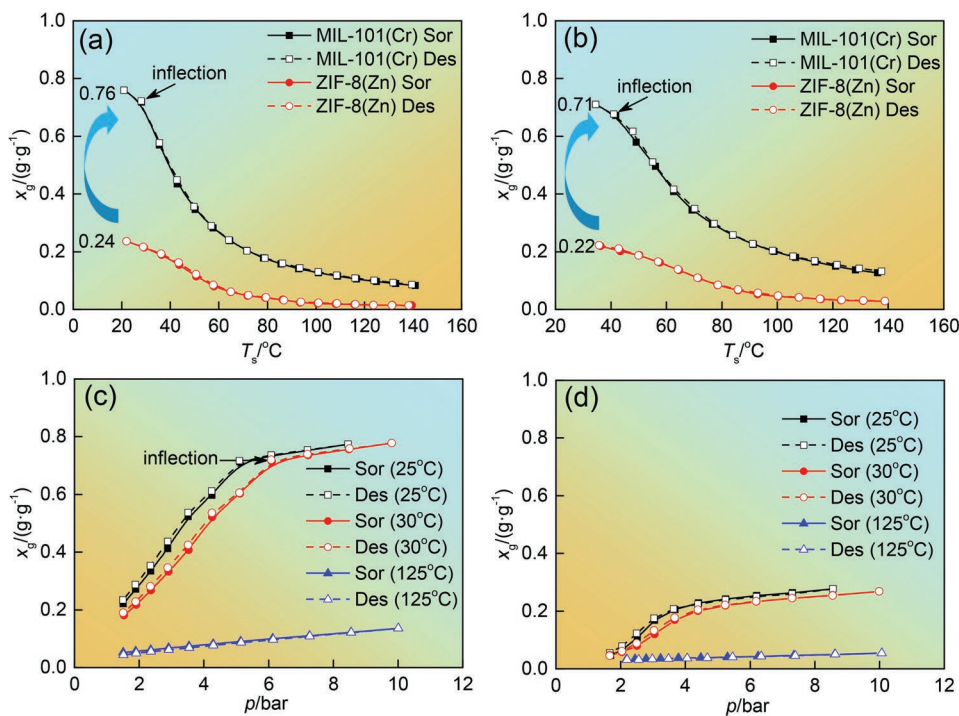
From the above characterization results, it is deduced that the ammonia sorption capacities of ZIF-8(Zn) and MIL-101(Cr) are contributed by their pore structures. Even though the porosity of MIL-101(Cr) is reduced during the pretreatment process under ammonia atmosphere, its remained porosity may be maintained during cyclic test to ensure the stable ammonia sorption capacity. Both chemisorption and pore structure

are beneficial for the ammonia sorption capacity of UiO-66(Zr), while the porosity of Cu-BTC is fully destroyed and its ammonia sorption capacity may be maintained by chemisorption on unsaturated metal sites.

The detailed characterization results of MIL-100(Fe), NU-1000(Zr) and DUT-67(Zr) exhibiting poor ammonia sorption stability before and after ammonia sorption are summarized in Figures S2–S5, Supporting Information. All of these MOFs lost their crystallinity, morphology, BET surface area, total pore volume and pore size. New bonds in FT-IR spectra and decreased ammonia uptake of MIL-100(Fe) and DUT-67(Zr) suggest that irreversible chemisorption occurred between NH_3 and MIL-100(Fe)/DUT-67(Zr), while no new bond in FT-IR spectra of NU-1000(Zr) means that the ammonia sorption capacity of NU-1000(Zr) was only contributed by its pore structure. Only MIL-101(Cr), ZIF-8(Zn), Cu-BTC, and UiO-66(Zr) with good ammonia sorption stability are taken into consideration in following sections.

3.2. Ammonia Sorption Thermodynamics of MOFs

Under the premise of acceptable ammonia sorption stability, negligible sorption hysteresis and large sorption capacity are the preferable characteristics for pursing high-performance thermal energy storage. As presented in **Figure 7**a,b, the sorption hysteresis of ZIF-8(Zn) was negligible, while its maximum ammonia sorption capacity was limited within 0.24 g g^{-1}, which was much lower than commonly used halides such as $MnCl_2$ (0.54 g g^{-1}) and $CaCl_2$ (0.92 g g^{-1}). Besides the high ammonia stability, MIL-101(Cr) had both the large maximum sorption capacity up to 0.76 g g^{-1} and negligible sorption

ADVANCED
SCIENCE NEWS
www.advancedsciencenews.com

NANO · MICRO
small
www.small-journal.com

Figure 7. Thermodynamics of candidate MOFs: isobars at a) 6.1 bar and b) 11.7 bar, isotherms of c) MIL-101(Cr) and d) ZIF-8(Zn).

hysteresis. Figure 7c,d show adsorption/desorption isotherms of MIL-101(Cr) and ZIF-8(Zn) at 25, 30, and 125 °C, respectively, in which no remarkable hysteresis was observed. Meanwhile, the obvious inflection point exists for MIL-101(Cr), at which its sorption state was approaching the maximum sorption capacity. MIL-101(Cr) and ZIF-8(Zn) can be fully recovered after the ammonia sorption experiments since their ammonia isotherms were recyclable. Meanwhile, the morphology of MIL-101(Cr) and ZIF-8(Zn) did not show any obvious change.

Since MIL-101(Cr) owns excellent ammonia sorption performance compared with other selected MOFs, the experimental result of UV–Vis absorption spectra of MIL-101(Cr) before and after ammonia adsorption is carried out to provide insights into the interactions between ammonia and Cr^{3+}. MIL-101(Cr) shows absorption in the UV range, which is caused by π–π^* bond from the frameworks of terephthalic acid, while the visible absorption at 430 and 590 nm could be attributed to the d-d orbital transition of Cr^{3+} (Figure S6, Supporting Information). After ammonia adsorption, visible absorption is blue-shifted (at 395 and 570 nm), which is caused by the reduction of unsaturated metal sites after the coordination of unsaturated Cr^{3+} and ammonia.[47] Such a phenomenon proves that Cr^{3+} reacts with ammonia which is effective for improving ammonia sorption performance.

The results of isobars of Cu-BTC and UiO-66(Zr) are presented in Figure S7, Supporting Information. The obvious hysteresis in ammonia adsorption/desorption isobars of Cu-BTC suggests that both the higher desorption temperature and lower adsorption temperature are required regardless of its recyclability at ammonia atmosphere, which is unfavorable for the thermal energy utilization efficiency. The presence of hysteresis of Cu-BTC-NH_3 working pair may be caused by both

the chemisorption between unsaturated metal (copper) sites of Cu-BTC and ammonia and the chemical reaction between Cu-BTC and ammonia, leading to the irreversible desorption process. The maximum sorption capacity and cycle sorption capacity (less than 0.15 g g^{-1}) of UiO-66(Zr) were the smallest with non-ignorable hysteresis area. The isotherms of Cu-BTC and UiO-66(Zr) at 30 °C also presented evident hysteresis areas (Figure S8, Supporting Information). The hysteresis area of Cu-BTC was so large that the sorption capacity could not return to the initial point after one isothermal cycle (material degradation). Meanwhile, the octahedral structure of Cu-BTC was destroyed after ammonia sorption. UiO-66(Zr) still maintained a hexahedral structure, while the surface became rough and defective after ammonia sorption. These facts prove that Cu-BTC and UiO-66(Zr) cannot be fully recovered. Therefore, Cu-BTC and UiO-66(Zr) are not considered anymore for thermal energy storage.

3.3. Thermodynamics Comparison between MOF-Ammonia and MOF-Water

Results of ammonia sorption thermodynamics of MOF-ammonia working pairs show that MIL-101(Cr)-ammonia is the optimal working pair, so it is compared with MIL-101(Cr)-water working pair, which exhibits type S isotherms.[48] As presented in **Figure 8**, the evaporation temperature requirement of MIL-101(Cr)-water working pair is critical for pursuing high sorption capacity. For instance, when p/p_0 ranges from 0.45 to 0.35 (corresponding evaporation temperature of water equals to 12.2 and 8.4 °C, respectively), the sorption capacity of MIL-101(Cr)-water working pair will drop from 1.07 to 0.23 g g^{-1}
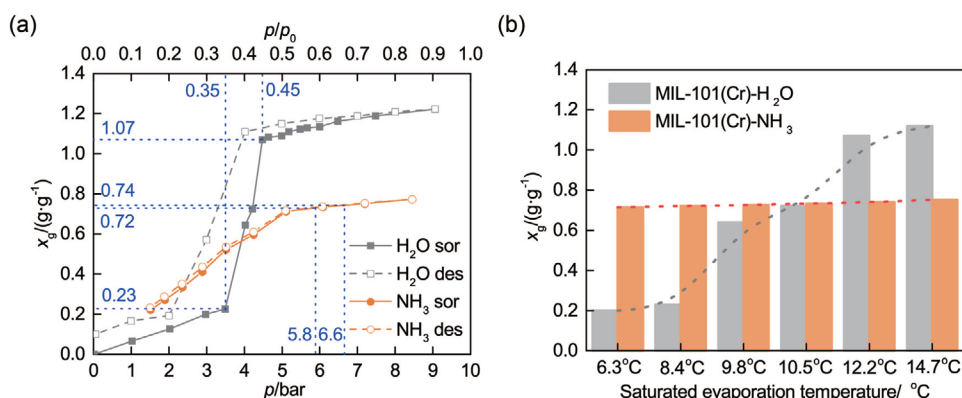
Figure 8. Comparison of MIL-101(Cr)-water working pair and MIL-101(Cr)-ammonia working pair: a) isotherms at 25 °C, b) sorption capacity at corresponding saturated evaporation temperature.

(Figure 8a). However, the sorption capacity of MIL-101(Cr)-ammonia working pair will range from 0.74 to 0.72 g g^{-1} with the same variation of evaporation temperature (corresponding evaporation pressure of ammonia equals to 6.6 and 5.8 bar, respectively). Deduced from Figure 8a, Figure 8b directly shows that MIL-101(Cr)-ammonia working pair presents much higher working capacity than MIL-101(Cr)-water working pair under the critical working condition of low evaporation temperature in winter.

Similarly, the desorption process of MIL-101(Cr)-water working pair at high condensation temperature ≈30 °C is also quite difficult. Existing literature only reports the experimental desorption process with condensation temperature at 10 °C,[49] which is not suitable for summer. Furthermore, MIL-101(Cr)-water working pair owns large hysteresis because the pore diameter of MIL-101(Cr) (34/29 Å) is much larger than the D_c of water (21 Å),[50] which will make feasibility worse for critical conditions of high condensation temperature and low evaporation temperature and largely influence its thermal energy storage density.

In the following section the desorption process with high condensation temperature of 30 °C and adsorption process with low evaporation temperature of 10 °C are analyzed in order to research the adaptability of MOF-ammonia working pairs under critical conditions.

3.4. Potential Application of MOFs in Thermal Energy Storage

3.4.1. Thermodynamic Cycle

The basic working principle of thermal energy storage can be presented by the isosteric cycle diagram shown in **Figure 9**a.

1) Isosteric heating process (I–II): In this stage, the sorbent is heated from T_1 to T_2 when adsorbing sensible heat (q_{s1-2}), but the sorption capacity can keep saturated (x_{max}) since the local pressure of sorbent is still lower than the constraint pressure at p_{con}.
2) Isobaric desorption process (II–III): Continuing heating sorbent from T_2 to T_3 will lead to desorption from x_{max} to x_{min} with ammonia condensed into the two-phase ammonia storage tank, releasing condensing heat (q_{con}), and the input energy is consumed by both sensible heat (q_{s2-3}) and desorption heat (q_{des}) of the sorbent.
3) Isosteric cooling process (III–IV): After desorption, the sorbent is cooled from T_3 to T_4 with sensible heat (q_{s3-4}) released, but adsorption will not occur until the local pressure of sorbent achieves the constraint pressure at p_{eva}.
4) Isobaric adsorption process (IV–I): Decreasing sorbent temperature from T_4 to T_1 will cause continuous ammonia evaporation (q_{eva}) from the ammonia storage tank to sorption bed
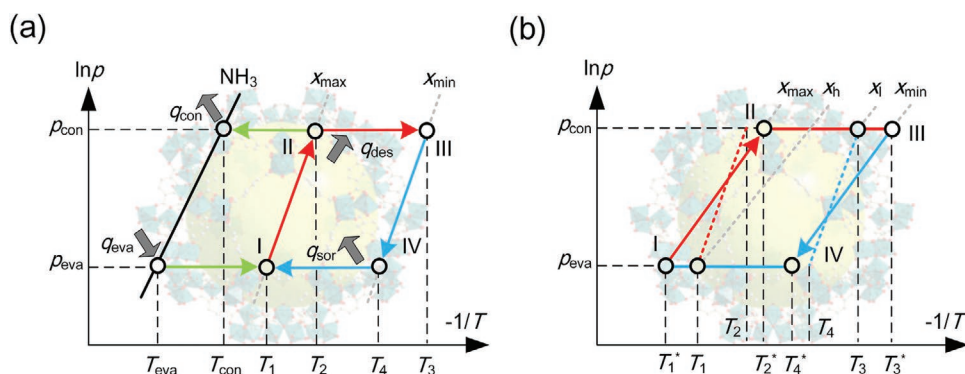
Figure 9. Isosteric diagram of sorption cycle, including the saturated state of ammonia (black line), sorption capacity (grey dashed lines), ammonia flow (green lines), and sorbent state variation (red and blue lines). a) single-stage sorption cycle, b) the impact of hysteresis on adsorption/desorption processes.

**ADVANCED
SCIENCE NEWS**

www.advancedsciencenews.com

**NANO · MICRO
small**

www.small-journal.com

for capacity back to x_{max}, and the output energy is the sum of sensible heat (q_{s4-1}) and sorption heat (q_{sor}) of the sorbent.

The impact of hysteresis on sorption process is depicted in Figure 9b. Since the temperature for initial/complete adsorption requires decreasing from T_4 to T_4*/T_1 to T_1* and the temperature for initial/complete desorption needs increasing from T_2 to T_2*/T_3 to T_3*, the maximum and minimum sorption capacity should be updated. Thus, the cycle sorption capacity will drop down to ($x_h - x_1$) if the sorbent temperature still ranges between T_1 and T_3, resulting in the much lower output energy compared with the theoretical value without hysteresis.

3.4.2. Thermodynamic Models

Thermal energy storage density (E_{sl}) and coefficient of performance of thermal energy storage (COP_{sl}) are defined as follows:

$$E_{s1} = q_{sor} = \frac{1}{M}\int_{x_{IV}}^{x_I} \Delta H_{sor}(x)\,dx = \frac{x_I - x_{IV}}{M}\overline{\Delta H_{sor}} \tag{2}$$

$$q_{des} = \frac{1}{M}\int_{x_{III}}^{x_{II}} \Delta H_{des}(x)\,dx = \frac{x_{II} - x_{III}}{M}\overline{\Delta H_{des}} \tag{3}$$

$$q_{si-j} = c_{sor}\left|T_j - T_i\right| \tag{4}$$

$$COP_{sl} = \frac{q_{sor}}{q_{sl-2} + q_{s2-3} + q_{des}} \tag{5}$$

where c_{sor} is the specific heat capacity of sorbent (kJ kg^{-1} K^{-1}), M is the relative molecular mass of ammonia (kg mol^{-1}), ΔH_{NH3} is the absolute value of enthalpy change of ammonia evaporation/condensation (kJ mol^{-1}) with detailed values in Figure S9, Supporting Information, $\Delta H_{sor}(x)$ and $\Delta H_{des}(x)$ are the isosteric adsorption and desorption enthalpy of sorbent (kJ mol^{-1}) depending on the sorption capacity, $\overline{\Delta H_{sor}}$ and $\overline{\Delta H_{des}}$ are the average isosteric adsorption and desorption enthalpy of sorbent during the whole process.

The isosteric adsorption enthalpy and desorption enthalpy can be considered as the same value for MOFs without obvious sorption hysteresis, which can be calculated from isotherms at various temperatures (Figure 7c,d), as shown in Equation (6) which is derived from van't Hoff equation.

$$\Delta H_{sor}(x) = \Delta H_{des}(x) = R\left(\frac{\partial lnp}{\partial(1/T_s)}\right)_x \tag{6}$$

As shown in Figure S10, Supporting Information, the isosteric enthalpy of MIL-101(Cr) keeps dropping from 41.2 to 26.2 kJ mol^{-1} with the increased sorption capacity, while ZIF-8(Zn) has a maximum isosteric enthalpy of 40.2 kJ mol^{-1} at ≈0.25 g g^{-1}. As employing specific heat capacity of 1 kJ kg^{-1} K^{-1} for all investigated MOFs will not significantly influence their thermodynamic performance (≈5% deviation in COP),[23,51] we use the specific heat capacity of 1 kJ kg^{-1} K^{-1} for MOFs in this work.

3.4.3. Thermodynamic Performance Evaluation

The operational conditions used to assess the thermodynamic performance are listed in Table S2, Supporting Information. When examining the effect of desorption temperature (T_{des}) on thermodynamic performance of MOF-based energy systems, adsorption temperature (T_{sor}) is kept constant that is identical to the condensing temperature (T_{con}). On the other hand, when investigating the influence of T_{sor}, T_{des} is fixed at 100 °C which is the typical heating temperature of the solar collector. Taking MIL-101(Cr) as an example, the calculation details of cycle sorption capacity (Δx) is presented in Figure S11, Supporting Information, which is greatly affected by the operational conditions.

The impact of T_{des} and T_{sor} on E_{sl}, Δx and COP_{sl} of MIL-101(Cr) and ZIF-8(Zn) are shown in **Figure 10**a,b. Both E_{sl} and Δx are larger at the higher T_{des} and the lower T_{sor} due to the more adequate reaction. E_{sl}, Δx and COP_{sl} of MIL-101(Cr)-based system are higher than ZIF-8(Zn)-based one throughout the operation conditions, which is caused by the comprehensive effect of the large average isosteric enthalpy and sorption capacity of MIL-101(Cr). E_{sl} of MIL-101(Cr) can reach over 1000 kJ kg^{-1} with T_{des} at ≈100 °C and T_{sor} at 30 °C, which is comparable with most halides, and the effective working temperature range of MIL-101(Cr) is much wider than those halides.[52] Furthermore, COP_{sl} of MIL-101(Cr) can maintain above 0.8 within a
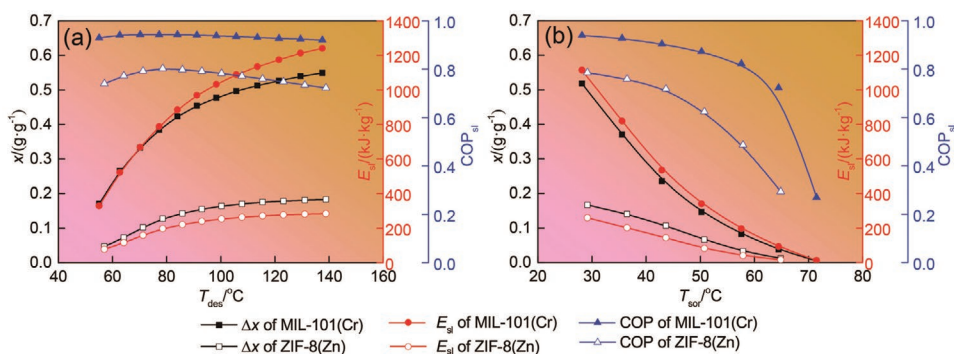
Figure 10. The impact of a) T_{des} and b) T_{sor} on cycle sorption capacity (black lines), thermal energy storage density (red lines) and coefficient of performance (blue lines) of MIL-101(Cr) (solid symbols) and ZIF-8(Zn) (hollow symbols) under conditions.

**ADVANCED
SCIENCE NEWS**

www.advancedsciencenews.com

NANO · MICRO

small

www.small-journal.com

wide temperature zone except for $T_{sor} > 60\ °C$. Therefore, MIL-101(Cr) is more suitable for ammonia-based thermal energy storage than ZIF-8(Zn).

4. Conclusion

The potential of MOF-ammonia working pairs in thermal energy storage has been critically assessed in this work. Among seven selected MOFs, MIL-101(Cr), ZIF-8(Zn), Cu-BTC, and UiO-66(Zr) exhibit outstanding ammonia sorption stability after nine ammonia sorption cycles. Even though the crystalline structure of Cu-BTC has been disrupted after ammonia sorption, it still maintains the stable ammonia sorption capacity contributed by the chemical reaction with ammonia. However, the remarkable sorption hysteresis in the adsorption/desorption isobars of Cu-BTC and UiO-66(Zr) greatly limit their application. In contrast, ZIF-8(Zn) exhibits the highest stability among all selected MOFs and negligible sorption hysteresis, but its low ammonia uptake is not comparable with MIL-101(Cr). Even though the BET surface area of MIL-101(Cr) is decreased after ammonia sorption, it exhibits high ammonia sorption stability and the largest ammonia sorption capacity of $0.76\ g\ g^{-1}$. In addition, almost no sorption hysteresis is identified in both ammonia sorption isobars and isotherms of MIL-101(Cr), reducing the decline of thermal energy storage grade and efficiency. Meanwhile, MIL-101(Cr)-ammonia working pair does not exhibit type S isotherms, solving the common problem of huge reduction of sorption capacity for MIL-101(Cr)-water working pair under critical conditions of low evaporation temperature and high condensation temperature. Compared with MIL-101(Cr)-water working pair, MIL-101(Cr)-ammonia working pair improves the sorption capacity by over three times (from 0.23 to $0.72\ g\ g^{-1}$) with evaporation temperature lower than $8.4\ °C$. Meanwhile, MIL-101(Cr)-ammonia working pair also shows excellent desorption performance at high condensation temperature of $30\ °C$. Furthermore, MIL-101(Cr) exhibits the remarkably high thermal energy storage density of above $1200\ kJ\ kg^{-1}$ and coefficient of thermal energy storage of above 0.8 compared with ZIF-8(Zn). The excellent performance of MIL-101(Cr)-ammonia shows that it possesses a great potential in thermal energy storage especially for critical conditions with low evaporation temperature and high condensation temperature.

Results reveal that Cr^{3+} is the key factor in ammonia capture and maintaining the structural stability of MIL-101. For further research, MIL-101 with different trivalent metal ions such as Al^{3+} will be studied to explore the interaction between metal ions and ammonia sorption.

5. Experimental Section

Materials: The synthetic procedures of MIL-101(Cr),[53] MIL-100(Fe),[54] ZIF-8(Zn),[55] Cu-BTC,[56] UiO-66(Zr),[57] NU-1000(Zr),[58] and DUT-67(Zr)[59] were in accordance to literature, with details provided in Supporting Information S1.

Characterizations: The PXRD patterns were measured under room temperature and air environment, by a X'Pert PRO MPD X-ray diffractometer from PANalytical B.V. (Netherlands) using Cu Kα radiation ($\lambda = 1.540598$ Å) within the 2θ range from 2° to 15° with a step size of 0.016711° and scan rate of 0.12 s per step. The FT-IR spectra were obtained under room temperature and air environment, using a VERTEX 70 FT-IR spectrometers from Bruker (Germany) with spectral resolution of 2 cm^{-1} on KBr mixed pellet. The collected spectra ranged from 4000 to 400 cm^{-1} and for each spectrum 32 co-added scans were obtained. SEM images were conducted using a Nova NanoSEM 450 SEM instrument from FEI (Netherlands) on the samples previously dried and sputter-coated with a gold layer at an accelerating voltage of 30 kV. TEM images were carried out using a Tecnai G2 20 TEM instrument from FEI (Netherlands) on the samples previously dispersed with ethanol. The nitrogen (N$_2$) adsorption isotherms were measured at 77 K on a Quantachrome Autosorb-iQ2 gas analyzer (US). After vacuum degassing at 393 K for 24 h before measurement, the sample tube was put into the cold well of 77 K and a fixed amount of N$_2$ was filled. The Brunauer–Emmett–Teller (BET) surface area was determined with a relative pressure (p/p_0) range of 0.08–0.25 on N$_2$ adsorption isotherm based on the BET theory, and the total pore volume was determined at $p/p_0 = 0.99$. PSD was obtained by using Saito–Foley and non-local density functional theory methods. UV–Vis spectra were measured with a Lamda 950 (China) spectrometer in reflection mode. The ammonia sorption stability and isobars/isotherms of MOFs were tested by the Rubotherm balance (TA Instruments, US) with resolution of 20 μg. The sample was put in a steel basket suspending in a sealed steel chamber, whose temperature was controlled through thermal radiation via the circulation oil. The oil temperature was controlled by the thermostatic bath (SE-6, JULABO, Germany) with temperature accuracy of 0.01 K. A PT100 temperature sensor with the accuracy of 0.1 K was located beneath the basket to monitor the temperature of the sorbent. The measuring chamber was connected with an ammonia tank which acted as the condenser/evaporator, whose temperature was controlled by the thermostatic glycol water bath (F32-ME, JULABO, Germany) with 0.01 K temperature accuracy. The working pressure of the measuring chamber was under the saturated pressure of ammonia and was detected by an absolute pressure sensor (DPI-282, Druck, UK) with the precision of 0.04%. In details, for ammonia adsorption/desorption stability test, the temperature of ammonia tank was kept constant at 10 °C for obtaining a constant pressure of 6.1 bar, while the temperature of thermostatic oil bath was controlled changing from 20 to 180 °C periodically. For isobaric test, the temperature of ammonia tank was set to 10 °C/30 °C at 6.1 bar/11.7 bar, while the temperature of thermostatic oil bath was increased from 20/40 to 180 °C for desorption process and decreased from 180 to 20 °C/40 °C for adsorption process with temperature interval of 10 °C maintaining 3 h per step. For isotherms test, the sorbent temperature was kept constant at 25 °C/30 °C/125 °C, respectively, while the temperature of ammonia tank varied from –25 to 25 °C for adsorption process and from 25 to –25 °C for desorption process with a temperature interval of 5 °C and maintained 1.5–3 h per step. In this case, the pressure could be controlled between 1.5 and 10.0 bar.

Supporting Information

Supporting Information is available from the Wiley Online Library or from the author.

Acknowledgements

Conflict of Interest

The authors declare no conflict of interest.

Data Availability Statement

Research data are not shared.

Keywords

ammonia, metal–organic frameworks, stability, thermal energy storage

[1] Xinhua, Scientific Community Calls for Global Cooperation to Meet Scientific Challenges, http://www.china.org.cn/china/Off_the_Wire/2019-10/17/content_75309434.htm, (accessed: March 2021).

[2] I. Gur, K. Sawyer, R. Prasher, *Science* **2012**, *335*, 1454.

[3] C. Forman, I. Muritala, R. Pardemann, B. Meyer, *Renewable Sustainable Energy Rev.* **2016**, *57*, 1568.

[4] M. Elashmawy, *Desalination* **2020**, *473*, 114182.

[5] S. Wu, T. Yan, Z. Kuai, W. Pan, *Energy Storage Mater.* **2020**, *25*, 251.

[6] Q. Wang, Y. Liu, J. Luo, S. Wang, J. Tang, X. Xu, G. Chen, *J. Cleaner Prod.* **2020**, *277*, 123303.

[7] J. Xu, J. Chao, T. Li, T. Yan, S. Wu, M. Wu, B. Zhao, R. Wang, *ACS Cent. Sci.* **2020**, *6*, 1542.

[8] G. An, Y. Zhang, L. Wang, B. Zhang, *J. Mater. Chem. A* **2020**, *8*, 11849.

[9] L. Wang, R. Wang, R. Oliveira, *Renewable Sustainable Energy Rev.* **2009**, *13*, 518.

[10] L. Wang, R. Wang, J. Wu, K. Wang, *Sci. China, Ser. E* **2004**, *47*, 173.

[11] L. Jiang, L. Wang, Z. Jin, R. Wang, Y. Dai, *Int. J. Therm. Sci.* **2013**, *71*, 103.

[12] N. Yu, R. Wang, L. Wang, *Prog. Energy Combust. Sci.* **2013**, *39*, 489.

[13] H. Li, K. Wang, Y. Sun, C. Lollar, J. Li, H. Zhou, *Mater. Today* **2018**, *21*, 108.

[14] F. Xiao, G. Xu, C. Sun, M. Xu, W. Wen, Q. Wang, M. Gu, S. Zhu, Y. Li, Z. Wei, X. Pan, J. Wang, K. Amine, M. Shao, *Nano Energy* **2019**, *61*, 60.

[15] Y. Li, X. Zhu, S. Li, Y. Jiang, M. Hu, Q. Zhai, *ACS Appl. Mater. Interfaces* **2019**, *11*, 11338.

[16] J. Yang, Y. Yang, *Small* **2020**, *16*, 1906846.

[17] A. Howarth, Y. Liu, P. Li, Z. Li, T. Wang, J. Hupp, O. Farha, *Nat. Rev. Mater.* **2016**, *1*, 15018.

[18] A. Rieth, A. Wright, M. Dincă, *Nat. Rev. Mater.* **2019**, *4*, 708.

[19] S. Henninger, F. Habib, C. Janiak, *J. Am. Chem. Soc.* **2009**, *131*, 2776.

[20] H. Kim, S. Yang, S. Rao, S. Narayanan, E. Kapustin, H. Furukawa, A. Umans, O. Yaghi, E. Wang, *Science* **2017**, *356*, 430.

[21] S. Wang, J. Lee, M. Wahiduzzaman, J. Park, M. Muschi, C. Martineau-Corcos, A. Tissot, K. Cho, J. Marrot, W. Shepard, *Nat. Energy* **2018**, *3*, 985.

[22] K. Cho, D. Borges, U. Lee, J. Lee, J. Yoon, S. Cho, J. Park, W. Lombardo, D. Moon, A. Sapienza, G. Maurin, J. Chang, *Nat. Commun.* **2020**, *11*, 5112.

[23] M. de Lange, K. Verouden, T. Vlugt, J. Gascon, F. Kapteijn, *Chem. Rev.* **2015**, *115*, 12205.

[24] S. Chaemchuen, X. Xiao, N. Klomkliang, M. Yusubov, F. Verpoort, *Nanomaterials* **2018**, *8*, 661.

[25] N. Makhanya, B. Oboirien, J. Ren, N. Musyoka, A. Sciacovelli, *J. Energy Storage* **2021**, *34*, 102179.

[26] J. Gao, L. Wang, P. Gao, G. An, Z. Wang, S. Xu, R. Wang, *Int. J. Refrig.* **2019**, *98*, 129.

[27] D. Lee, J. Jamir, G. Peterson, G. Parsons, *Small* **2019**, *15*, 1805133.

[28] D. Kim, D. Kang, M. Kang, J. Lee, J. Choe, Y. Chae, D. Choi, H. Yun, C. Hong, *Angew. Chem., Int. Ed.* **2020**, *59*, 22531.

[29] G. Han, C. Liu, Q. Yang, D. Liu, C. Zhong, *Chem. Eng. J.* **2020**, *401*, 126106.

[30] Q. Mi, D. Zhang, X. Zhang, D. Wang, *J. Alloys Compd.* **2021**, *860*, 158252.

[31] M. Yao, X. Lv, Z. Fu, W. Li, W. Deng, G. Wu, G. Xu, *Angew. Chem., Int. Ed.* **2017**, *56*, 16510.

[32] J. Zhang, J. Ouyang, Y. Ye, Z. Li, Q. Lin, T. Chen, Z. Zhang, S. Xiang, *ACS Appl. Mater. Interfaces* **2018**, *10*, 27465.

[33] A. Rieth, Y. Tulchinsky, M. Dinca, *J. Am. Chem. Soc.* **2016**, *138*, 9401.

[34] A. Rieth, M. Dinca, *J. Am. Chem. Soc.* **2018**, *140*, 3461.

[35] N. Nijem, K. Fürsich, H. Bluhm, S. Leone, M. Gilles, *J. Phys. Chem. C* **2015**, *119*, 24781.

[36] C. Petit, B. Mendoza, T. Bandosz, *Langmuir* **2010**, *26*, 15302.

[37] H. Jasuja, G. Peterson, J. Decoste, M. Browe, K. Walton, *Chem. Eng. Sci.* **2015**, *124*, 118.

[38] J. Canivet, A. Fateeva, Y. Guo, B. Coasne, D. Farrusseng, *Chem. Soc. Rev.* **2014**, *43*, 5594.

[39] B. Coasne, K. Gubbins, R. Pellenq, *Adsorption* **2005**, *11*, 289.

[40] X. Sun, Q. Xia, Z. Zhao, Y. Li, Z. Li, *Chem. Eng. J.* **2014**, *239*, 226.

[41] Y. Chen, F. Zhang, Y. Wang, C. Yang, J. Yang, J. Li, *Microporous Mesoporous Mater.* **2018**, *258*, 170.

[42] T. Kajiwara, M. Higuchi, D. Watanabe, H. Higashimura, T. Yamada, H. Kitagawa, *Chem. - Eur. J.* **2014**, *20*, 15611.

[43] W. Morris, C. Doonan, O. Yaghi, *Inorg. Chem.* **2011**, *50*, 6853.

[44] G. Peterson, G. Wagner, A. Balboa, J. Mahle, T. Sewell, C. Karwacki, *J. Phys. Chem. C* **2009**, *113*, 13906.

[45] Y. Chen, B. Shan, C. Yang, J. Yang, J. Li, B. Mu, *J. Mater. Chem. A* **2018**, *6*, 9922.

[46] D. Britt, D. Tranchemontagne, O. Yaghi, *Proc. Natl. Acad. Sci. U. S. A.* **2008**, *105*, 11623.

[47] X. Si, L. Sun, F. Xu, C. Jiao, F. Li, S. Liu, J. Zhang, L. Song, C. Jiang, S. Wang, Y. Liu, Y. Sawada, *Int. J. Hydrogen Energy* **2011**, *36*, 6698.

[48] J. Yan, Y. Yu, C. Ma, J. Xiao, Q. Xia, Y. Li, Z. Li, *Appl. Therm. Eng.* **2015**, *84*, 118.

[49] A. Permyakova, S. Wang, E. Courbon, F. Nouar, N. Heymans, P. D'Ans, N. Barrier, P. Billemont, G. De Weireld, N. Steunou, *J. Mater. Chem. A* **2017**, *5*, 12889.

[50] A. Khutia, H. Rammelberg, T. Schmidt, S. Henninger, C. Janiak, *Chem. Mater.* **2013**, *25*, 790.

[51] B. Mu, K. Walton, *J. Phys. Chem. C* **2011**, *115*, 22748.

[52] T. Li, R. Wang, J. Kiplagat, *AIChE J.* **2013**, *59*, 1334.

[53] G. Ferey, C. Mellot-Draznieks, C. Serre, F. Millange, J. Dutour, S. Surble, I. Margiolaki, *Science* **2005**, *309*, 2040.

[54] Y. Seo, J. Yoon, J. Lee, U. Lee, Y. Hwang, C. Jun, P. Horcajada, C. Serre, J. Chang, *Microporous Mesoporous Mater.* **2012**, *157*, 137.

[55] J. Cravillon, S. Munzer, S. Lohmeier, A. Feldhoff, K. Huber, M. Wiebcke, *Chem. Mater.* **2009**, *21*, 1410.

[56] Q. Wang, D. Shen, M. Bulow, M. Lau, S. Deng, F. Fitch, N. Lemcoff, J. Semanscin, *Microporous Mesoporous Mater.* **2002**, *55*, 217.

[57] A. Schaate, P. Roy, A. Godt, J. Lippke, F. Waltz, M. Wiebcke, P. Behrens, *Chem. - Eur. J.* **2011**, *17*, 6643.

[58] T. Wang, N. Vermeulen, I. Kim, A. Martinson, J. Stoddart, J. Hupp, O. Farha, *Nat. Protoc.* **2016**, *11*, 149.

[59] V. Bon, I. Senkovska, I. Baburin, S. Kaskel, *Cryst. Growth Des.* **2013**, *13*, 1231.